



Cite this: *Nanoscale Adv.*, 2019, **1**, 2718

## Physical mechanisms involved in the formation and operation of memory devices based on a monolayer of gold nanoparticle-polythiophene hybrid materials†

T. Zhang,<sup>a</sup> D. Guérin,<sup>a</sup> F. Alibart,<sup>a</sup> D. Troadec,<sup>a</sup> D. Hourlier,<sup>a</sup> G. Patriarche,<sup>ID c</sup> A. Yassin,<sup>b</sup> M. Ocafrain,<sup>b</sup> P. Blanchard,<sup>ID b</sup> J. Roncali,<sup>ID bd</sup> D. Vuillaume,<sup>ID a</sup> K. Lmimouni<sup>a</sup> and S. Lenfant<sup>ID \*a</sup>

Understanding the physical and chemical mechanisms occurring during the forming process and operation of an organic resistive memory device is a requisite for better performance. Various mechanisms were suggested in vertically stacked memory structures, but the analysis remains indirect and needs destructive characterization (e.g. analysis of the cross-section to access the organic layers sandwiched between electrodes). Here, we report a study on a planar, monolayer thick, hybrid nanoparticle/molecule device (10 nm gold nanoparticles embedded in an electro-generated poly(2-thienyl-3,4-(ethylenedioxy)thiophene) layer), combining *in situ* physical (scanning electron microscopy, physicochemical thermogravimetry and mass spectroscopy, and Raman spectroscopy) and electrical (temperature dependent current–voltage) characterization on the same device. We demonstrate that the forming process causes an increase in the gold particle size, almost 4 times larger than the starting nanoparticles, and that the organic layer undergoes a significant chemical rearrangement from an  $sp^3$  to  $sp^2$  amorphous carbon material. Temperature dependent electrical characterization of this nonvolatile memory confirms that the charge transport mechanism in the device is consistent with a trap-filled space charge limited current in the off state, with the  $sp^2$  amorphous carbon material containing many electrically active defects.

Received 6th May 2019  
Accepted 23rd May 2019

DOI: 10.1039/c9na00285e  
[rsc.li/nanoscale-advances](http://rsc.li/nanoscale-advances)

### 1. Introduction

Organic resistive random-access memories (ORRAMs) are promising as fundamental elements for the development of electronic organic circuitries<sup>1,2</sup> due to their various advantages, such as a simple and low cost fabrication process, light weight, mechanical flexibility and tunable materials properties. ORRAMs should present two non-volatile resistance states separated by at least 3 orders of magnitude.<sup>1,2</sup> These resistance

states can be read by measuring the current at a low voltage, and switched by applying a higher voltage sequence.

We have recently demonstrated<sup>3</sup> a hybrid memristive device based on a network of gold nanoparticles (GNPs) of 10 nm diameter connected by chains of a conjugated polymer. This molecule–GPN network was fabricated between two planar platinum electrodes a distance of 0.1 to 10  $\mu\text{m}$  apart. After preparation of GNPs functionalized with 10-(2-(3,4-ethylenedioxythiophene)thiophen-3-sulfanyl)decane-1-thiol molecules, *in situ* electropolymerization of the thiophene-ethylenedioxythiophene moieties allowed the formation of a polymer–GPN monolayer<sup>4</sup> (see the inset in Fig. 1b). As in many resistive memories,<sup>1</sup> a forming process is mandatory before operation. The forming process consists of 3–4 voltage sweeps between 0 and 20 V at a sweep rate of  $\sim$ 4 V  $\text{s}^{-1}$ . Then, the electrical properties of these formed devices (Fig. 1) showed systematically (i) a negative differential resistance (NDR) behavior with a peak/valley ratio of up to 17 at a voltage of 6–7 V and (ii) a memory effect behavior with an on/off ratio in the  $10^3$  to  $10^4$  range. The retention time for both states was stable for at least 24 h, and the device stability was demonstrated for 800 cycles by switching between the two states.<sup>3</sup> The devices showed

<sup>a</sup>Institute of Electronics Microelectronics and Nanotechnology (IEMN), CNRS, University of Lille, Avenue Poincaré, F-59652 Villeneuve d'Ascq, France. E-mail: stephane.lenfant@iemn.univ-lille1.fr

<sup>b</sup>MOLTECH-Anjou, CNRS, University of Angers, 2 Bd Lavoisier, Angers, F-49045, France

<sup>c</sup>Centre for Nanoscience and Nanotechnology (C2N), CNRS, University of Paris-Saclay, Route de Nozay, Marcoussis, F-91460, France

<sup>d</sup>Supramolecular Organic and Organometallic Chemistry Center Babes, Bolyai University, 11 Arany Janos str, 400028 Cluj-Napoca, Romania

† Electronic supplementary information (ESI) available: Cluster analysis by STEM after the forming process, model of transport applied on  $I$ – $V$  memory characteristics: variable range hopping model, thermionic emission limited conduction (TELC) model and additional  $I$ – $V$  curves for shorter devices. See DOI: 10.1039/c9na00285e



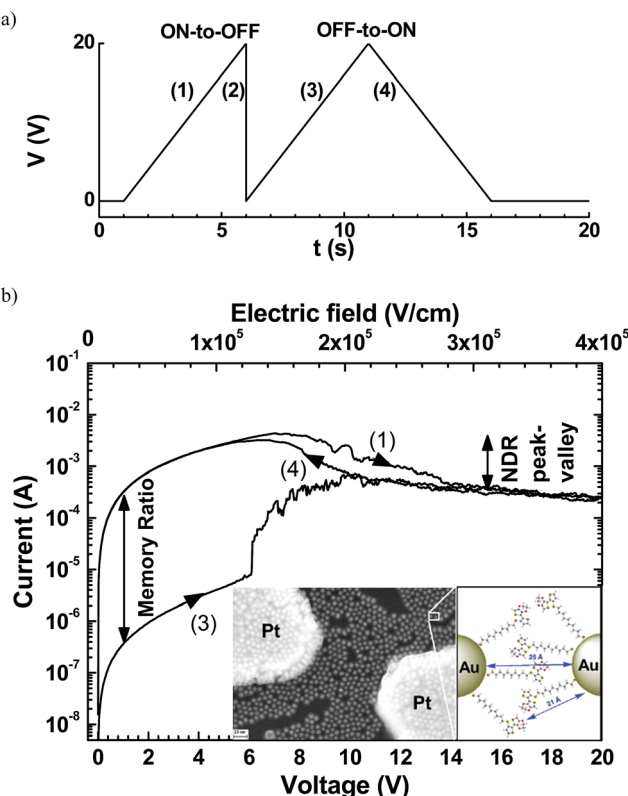


Fig. 1 (a) Typical voltage sequence for the memory behavior and (b) the corresponding  $I$ - $V$  curves for the ON-to-OFF and OFF-to-ON switches of a device after the forming process with a length  $L = 500$  nm and width  $W = 1$  mm. The current-voltage  $I$ - $V$  traces are numbered according to the voltage sequences shown in (a). Inset, SEM image of a network of functionalized-GNP monolayer on a nanogap platinum electrodes (electrode spacing  $L = 200$  nm and electrode width  $W = 100$  nm); bar scale represents 30 nm; and schematic magnified view of a GNP interspace from ref. 3. Reprinted from ref. 3, copyright American Chemical Society 2017.

no significant degradation in these 800 cycles between the ON and OFF states at a current ratio about  $10^3$ . Then, reading pulses of up to  $10^5$  s were applied to measure the ON and OFF currents. The results showed good data retention without current drift in this memory.<sup>3</sup> However, no clear physical mechanism was evidenced in previous studies.

Many studies on vertically stacked hybrid metal/organic-GNP/metal memories<sup>5–16</sup> have proposed various mechanisms, such as (i) the formation of metallic filaments;<sup>13,14,16,17</sup> (ii) electric field-induced charge transfer between organic materials and metallic nanoparticles;<sup>6,7</sup> (iii) the inhibition of charge injection by the space-charge field of trapped charges inducing a space charge limited current (SCLC)<sup>8,12,15</sup> and (iv) charge trapping/release in NP–organic composites<sup>6</sup> or in NPs associated with tunneling through the organic material.<sup>10</sup> However, these studies require destructive analysis, *e.g.* analysis of the cross-section to access the hybrid organic–NP layer between the metal electrodes for physicochemical studies.

In the present work, the advantage of a nanoscale monolayer thick planar structure placed between coplanar electrodes is that it makes it possible to characterize the physicochemical

properties and electrical structure of the active material on the same device and also during operation for a better understanding of the mechanisms responsible for the forming process and resistive switching memory. Another advantage is the ability to prevent metal diffusion during top electrode deposition, which can also flaw the results in vertically stacked devices. Furthermore, the *in situ* electropolymerization process allows better control over the organization of the conjugated polymer GNP hybrid material and finally the active layer remains accessible and can be studied by several techniques during voltage cycles in order to better understand the physics of the operation mechanisms.

Here, we report on the mechanisms involved in the formation (forming process) and operation of devices based on an organic/GNP network with a monolayer thickness. For this purpose, different characterization studies have been carried out, namely (i) scanning (SEM) and transmission (STEM) electron microscopy of the morphological changes during the forming process and operation; (ii) evaluating the effects of thermal annealing on the morphology of the GNP network; (iii) analysis of the organic ligand material at high temperature and (iv) studying the temperature dependence of the charge transport behaviors in the two resistance states.

## 2. Materials and methods

### Device fabrication

**Electrode fabrication.** Devices were processed using a standard electron beam lithography process. We used highly doped  $n^+$ -type silicon (resistivity 1–3  $\mu\Omega$  cm) covered with thermally grown 200 nm thick silicon dioxide (135 min at 1100 °C in the presence of  $2\text{ L min}^{-1}$  oxygen followed by a post-oxidation annealing at 900 °C in  $2\text{ L min}^{-1}$   $\text{N}_2$  for 30 min). The planar electrodes were patterned by electronic lithography using 10% MAA 17.5%PMMA 3% 495 K bilayer resists (with thicknesses of 510 nm and 85 nm respectively). Titanium/platinum (5/50 nm) was deposited by vacuum evaporation and lift-off. We fabricated electrodes with channel length  $L = 200$  nm to 1  $\mu\text{m}$  and channel width  $W = 100$  nm to 1000 nm.

**Functionalized GNPs.** The synthesis of the ligand 10-(2-(3,4-ethylenedioxythiophene)thiophen-3-sulfanyl)decane-1-thiol (**HS-C10-TEDOT**) was described elsewhere.<sup>4,18</sup> The synthesis of 10 nm capped-GNPs (inset in Fig. 1b) involves ligand exchange by treating 10 nm oleylamine-GNPs<sup>19</sup> with **HS-C10-TEDOT** giving **TEDOT-C10-S-GNPs**. It was previously shown that oleylamine ligands are easily substituted by thiols<sup>20–22</sup> (for more details on the synthesis see ref. 3).

**Deposition of the TEDOT-C10-S-GNPs monolayer.** Langmuir films of **TEDOT-C10-S-GNPs** were prepared following the method of Santhanam<sup>23</sup> by evaporating a solution of functionalized GNPs in 1,1,2,2-tetrachloroethane on the convex meniscus of a DI (deionized) water surface in a Teflon Petri dish. The transfer of the floating film on the substrate with lithographed electrodes was realized by dip coating. **TEDOT-C10-S-GNPs** form a rather well-organized monolayer on the surface (also called NPSAN: nanoparticle self-assembled network) as seen in the SEM image (inset in Fig. 1b). Statistical



analysis of the SEM image gives an average diameter of the GNPs of 9.3 nm, and an average spacing of 2.5–3.0 nm between the NPs in the network.<sup>3</sup> Comparison of these distances with the calculated length of 2.1 nm for the free ligand (MOPAC simulation, ChemOffice software) suggests that the ligand molecules are interdigitated (inset in Fig. 1b). X-ray photoelectron spectroscopy (XPS) of the deposited **TEDOT-C10-S-GNP** monolayer on large surface silicon (without electrodes), shows the chemical composition of **C10-TEDOT** adsorbates before electro-polymerization.<sup>3</sup> The good agreement between the theoretical and measured atomic ratios (S 2p/C 1s) demonstrates the successful grafting of **HS-C10-TEDOT** on GNPs.<sup>3</sup> No signal is detected in the N 1s region, proving the complete substitution of oleylamine ligands with **HS-C10-TEDOT**.

**Electropolymerization of TEDOT-C10-S-GNP monolayers.** The deposited monolayer of **TEDOT-C10-S-GNPs** on coplanar Pt electrodes (inset in Fig. 1b) was electropolymerized *in situ*, using Pt lithographed electrodes as the working electrodes to form a monolayer film of **pTEDOT-C10-S-GNPs** (p stands for polymerized). Electropolymerization of the monolayer was realized in potentiodynamic mode (electrolyte: 0.1 M NBu<sub>4</sub>PF<sub>6</sub> in CH<sub>2</sub>Cl<sub>2</sub> or CH<sub>3</sub>CN) by multiple scans at 100 mV s<sup>-1</sup> between -0.4 V and +1 V. This process leads to the development of a broad redox system centered at +0.7 V *vs.* Ag/AgCl in the cyclic voltammogram (CV). The stabilization of the CV after multiple scans (~20) suggests that all redox active **TEDOT** units have been coupled,<sup>4</sup> in agreement with previous results.<sup>18</sup>

Electrochemical experiments were performed with a Modulab potentiostat from Solartron Analytical. The substrate with lithographed electrodes was hermetically fixed at the bottom of a 0.2 mL Teflon cell containing the electrolyte solution. The counter electrode was a platinum wire of 0.5 mm diameter and an Ag/AgCl electrode was used as a reference.

### Electrical measurement setup

Electrical measurements were performed with an Agilent 4156C parameter analyzer in DC sweeping mode. We used a Carl Süss PM5 probe station in order to connect the Agilent 4156C and devices. All electrical measurements were performed under an inert atmosphere inside a dried nitrogen filled glove box (O<sub>2</sub> < 1 ppm, H<sub>2</sub>O < 1 ppm).

### Thermogravimetry coupled with mass spectrometry analysis (TGA/MS)

Thermogravimetric analysis (TGA) (Netzsch STA449F3 Jupiter apparatus) coupled with quadrupole mass spectrometry (MS) (Aëlos QMS403D, 70 eV, electron impact) through a heated silica capillary system (0.220 mm internal diameter) has been used to monitor the thermal degradation of organic polymers. TGA provides information related to the changes in the sample mass during the annealing process, whereas mass spectrometry offers a method of identifying the evolved volatile species. Before each experiment, the TGA system was first evacuated and then flushed with ultrahigh purity helium before starting heating. The experiments were carried out under a dynamic inert gas atmosphere (helium: 99.999 purity) with a flow rate of

90 cm<sup>3</sup> min<sup>-1</sup>. The samples were heated using a heating rate of 10°C min<sup>-1</sup>.

### Raman spectroscopy

Raman spectroscopy measurements were performed using a Horiba Jobin-Yvon LabRam®HR micro-Raman system combined with a 473 nm laser diode as the excitation source focused using a  $\times 100$  objective. The scattered light was collected using the same objective in the backscattering configuration, dispersed by a holographic grating of 1800 l mm<sup>-1</sup> and detected using a CCD camera.

### Annealing of pTEDOT-C10-S-GNP monolayers

Freshly prepared **pTEDOT-C10-S-GNP** monolayers were subjected to thermal annealing under a nitrogen atmosphere (instrument: JetFirst 200 from JIPELEC). The annealing temperature (from 423 to 623 K with 50 K steps) was attained in 40 s from ambient temperature, and maintained for 120 s. After annealing, the samples were cooled to ambient temperature in 180 s.

### Scanning electron microscopy (SEM)

SEM observation was carried out using an MEB Ultra 55 purchased from Carl Zeiss or by Focused Ion Beam Strata DB 235 from FEI. The accelerating beam voltage was fixed at 10 kV and 5 kV respectively.

### Scanning transmission electron microscopy (STEM) analysis

Cross-section lamellae for the different samples were prepared with a focused ion beam (FIB) microscope (FEI STRATA DB 235). Milling steps were performed at 30 kV with the current decreasing from 20 nA to 30 pA and lamella thickness decreasing from 6  $\mu$ m to less than 100 nm, followed by a final step at 5 kV and 30 pA to minimize amorphization. The transfer of the lamella samples to the TEM grid was done using a Kleindiek micromanipulator. The STEM observations of these cross-section lamellae were done on an FEI Titan Themis 200 microscope. This microscope is equipped with an aberration corrector on the probe (STEM mode) and a Super-X windowless EDX (4 quadrant SDD EDX detectors with a solid angle > 0.7 sr). The acceleration voltage was 200 kV and the probe current was about 50 pA with a half convergence angle of 17.6 mrad. The HAADF-STEM (high angle annular dark field) images were obtained on an annular dark field detector with a collection angle between 69 and 200 mrad.

## 3. Results and discussion

### Evolution of the morphology of the pTEDOT-C10-S-GNP monolayer during the forming process

After electropolymerization, a forming process is mandatory to form the **formed-pTEDOT-C10-S-GNP** monolayer and to “initialize” the device and observe the NDR and memory operation.<sup>3</sup> It consists of 3–4 voltage sweeps from 0 to 20 V with a sweep rate of ~4 V s<sup>-1</sup> applied to the coplanar electrodes. SEM images of the same device before and after the forming process



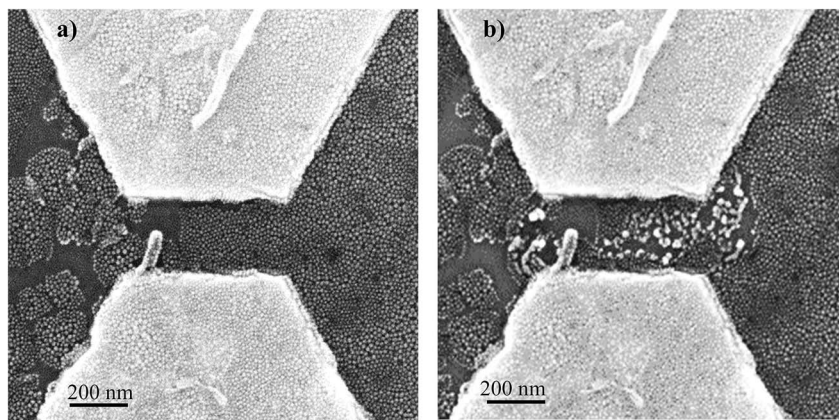


Fig. 2 SEM images of a pTEDOT-C10-S-GNP monolayer in a 200 nm channel length (GNP size 10 nm) before (a) and after (b) the forming process consisting of 3–4 voltage sweeps from 0 to 20 V (corresponding to an electric field maximum of  $100 \text{ MV m}^{-1}$ ).

reveal that the sudden current increase at a voltage of about 6–7 V (see Fig. 4 in ref. 3) during the forming process is associated to an irreversible modification of the morphology of the pTEDOT-C10-S-GNP monolayer between the two electrodes (Fig. 2). The SEM image obtained after the forming process (Fig. 2b) exhibits brighter gold clusters between the two electrodes. These clusters can be associated to reorganization or aggregation, or fusion of the GNPs under the electric field (around  $100 \text{ MV m}^{-1}$ ) applied between the electrodes and/or due to the current density induced heating during the forming process. For comparison, the dissolution/nucleation of embedded metallic clusters of platinum inside a  $\text{SiO}_2$  layer was measured under a higher electrical field between 300 and 500  $\text{MV m}^{-1}$ .<sup>24</sup> Here, the electric field is lower at  $100 \text{ MV m}^{-1}$  and can contribute to a lesser degree to the electromigration of the GNPs into the polymer. To analyze these morphological modifications more precisely, STEM analysis (see methods) has been performed along the cross-sections of the monolayer (along the dashed line in Fig. 3a and b). The image

recorded before the forming process (Fig. 3c) shows GNPs with  $\sim 10 \text{ nm}$  diameter, in agreement with the average value of  $9.3 \text{ nm}$  determined by the SEM analysis of the monolayer.<sup>3</sup> The image obtained after the forming process (Fig. 3d) clearly shows larger gold clusters with a diameter of up to  $40 \text{ nm}$ . This STEM image of the clusters shows that the clusters have a regular round shape rather than a less regular shape expected for the aggregation of several GNPs. Moreover, the high-resolution STEM image clearly reveals the monocrystalline structure of this cluster (see Fig. SI-1†). These observations suggest that the clusters are formed by the melting of several GNPs during the forming process rather than by their aggregation.

#### Evolution of the morphology of the pTEDOT-C10-S-GNP monolayer during thermal annealing

To understand the physical origin of the cluster formation and to estimate the temperature attained in the device during the forming process, pTEDOT-C10-S-GNP monolayers are annealed

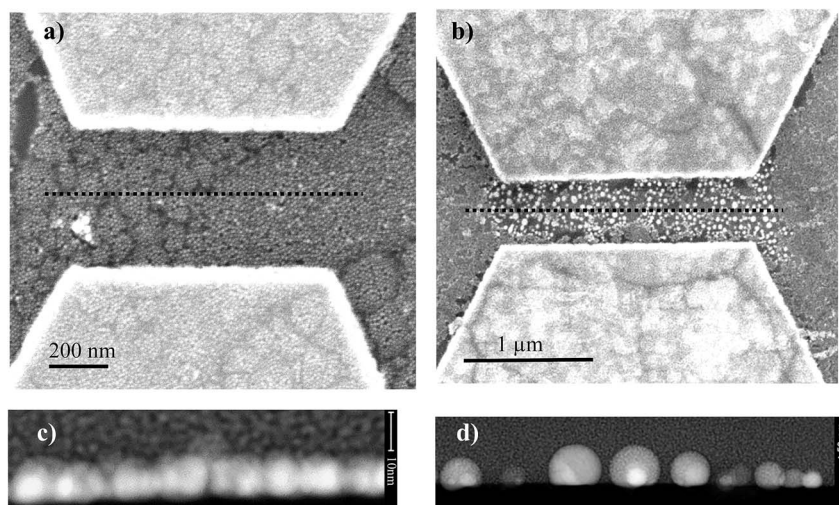


Fig. 3 Top: (a) SEM image of the pTEDOT-C10-S-GNP monolayer (GNP size 10 nm). (b) SEM image of a formed-pTEDOT-C10-S-GNP monolayer after the forming process. Bottom: corresponding HAADF-STEM images of the cross section between the electrode along the dotted line in SEM images, (c) for device before the forming process (scale bar 10 nm) and (d) after the forming process (scale bar 50 nm). The two devices have the same channel length of 500 nm.





at different temperatures from 423 to 623 K with 50 K steps (see methods) and imaged by SEM (Fig. 4). At lower temperatures (423 and 473 K), the GNPs present an average diameter of  $\sim$ 10 nm, in agreement with the average value of 9.3 nm determined by SEM and STEM analyses of the as-fabricated samples.<sup>3</sup> At 523 K, some clusters with a characteristic size between 20 and 40 nm appear in the monolayer. At higher temperatures, 573 K and 623 K, the number of these clusters increases dramatically. Finally, at 623 K, the majority of the GNPs melt to form these clusters.

The round shape and the size of the clusters formed by thermal annealing at 623 K are maintained after the forming process (Fig. 2b and 3b). This similarity suggests that during the forming process, the formation of clusters is caused by a local current-induced increase of the temperature in the monolayer (Joule effect).

We observe the beginning of the melting of GNPs at  $\sim$ 523 K (Fig. 4) while the melting point (mp) for bulk gold is 1337 K.<sup>25</sup> According to Buffat's thermodynamic model,<sup>26,27</sup> which correlates the mp of naked metal nanoparticles to their mean diameter, the mp for 9.3 nm diameter GNPs is predicted to be 1273 K. On the other hand, this value is drastically reduced when the GNP surface is coated with molecules<sup>28</sup> or silica.<sup>29</sup> These coating materials increase the surface energy value of the solid phase of the GNPs and reduce the mp, in agreement with Buffat's model. For example, Miyake *et al.*<sup>28</sup> have investigated the effect of thermal annealing on 2D superlattices (hexagonal packing) of GNPs coated with dodecane or octadecane-thiol. After thermal annealing at 423 K, the diameter of the dodecane coated GNPs increases from  $1.5 \pm 0.2$  nm to  $3.4 \pm 0.3$  nm. For coated GNPs with  $\sim$ 10 nm diameter, these authors estimate a mp of around 535 K which is close to the threshold temperature of 523 K observed in our experiments. Thus, we suggest that during the forming process a local temperature of at least 523 K is attained in the **pTEDOT-C10-S-GNP** monolayer leading

to the formation of clusters by the melting of the 10 nm diameter GNPs.

It was shown that in metal/oxide/metal coplanar structures for memory or memristive applications such as Ag/SiO<sub>2</sub>/Pt,<sup>30</sup> W/SiO<sub>2</sub>/Ag<sup>24</sup> or Pt/Ag nanoclusters in SiO<sub>2</sub>/Pt system,<sup>31</sup> the formation of metallic clusters may be caused by metal displacement or migration along the direction of the electric field between the metallic electrodes. However, to the best of our knowledge, no previous study mentioning the formation of clusters in organic bistable memories by a thermal effect has been reported so far.

#### Thermogravimetry coupled with mass spectrometry analysis (TGA/MS) and Raman spectroscopy

Since high temperatures (higher than 523 K) can be attained in the samples during the forming process, it was important to assess the thermal stability of organic ligands. Simultaneous thermogravimetry (TG) coupled with mass spectrometry (MS) was used to elucidate the thermal degradation/modification of organics. Two different organic compounds have been tested: (i) a conjugated polymer namely **p(TEDOT)** and (ii) 2 nm diameter GNPs functionalized with **HS-C10-TEDOT** (insets in Fig. 5). GNPs with 2 nm diameter instead of 10 nm have been chosen in order to improve the percentage in mass of the organic material, and therefore the sensitivity of analytical measurements (TG and MS). Indeed, with a surface density of 4.0 molecules per nm<sup>2</sup> determined by XPS,<sup>3</sup> the percentage in mass of organic material for nanoparticles of 2 nm and 10 nm diameter is estimated to be around 29% and 8%, respectively.

Fig. 5a and b show the TG/MS traces measured for the 2 nm diameter GNPs functionalized with the **HS-C10-TEDOT** ligand (powder was placed directly into a crucible), and for a thin film of **p(TEDOT)** (thickness of around 100  $\mu$ m) on a Si/Pt substrate prepared by electropolymerization of **TEDOT** monomers in a solution unit.<sup>32</sup> For TG/MS and Raman analyses of the **p(TEDOT)** film, we use the **TEDOT** molecule without the

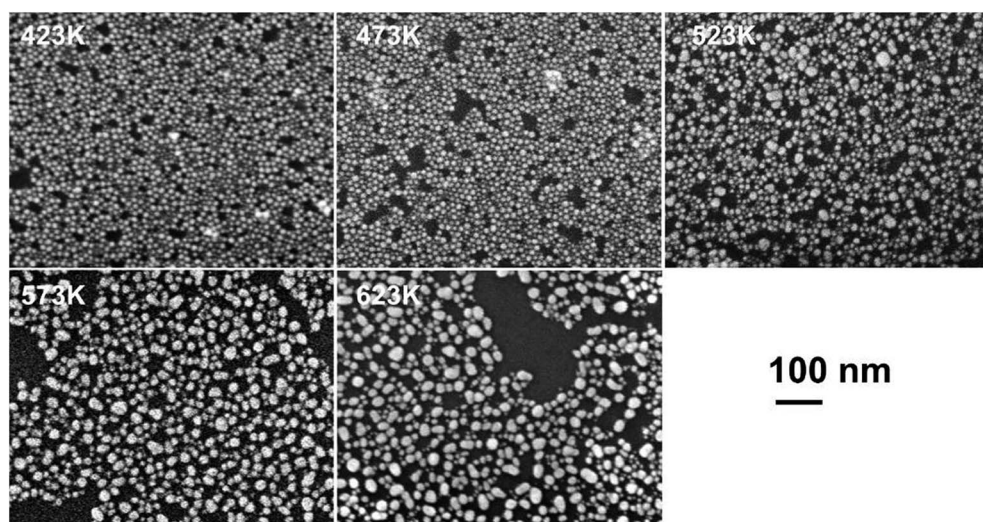


Fig. 4 SEM images of a **pTEDOT-C10-S-GNP** monolayer after thermal annealing at different temperatures from 423 to 623 K with 50 K steps. Images were acquired in the gap electrode.

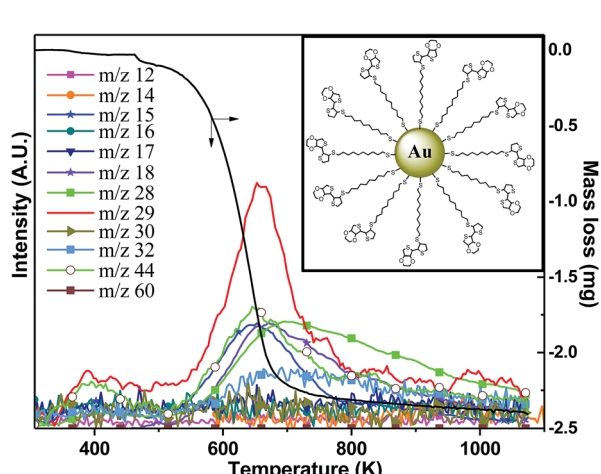


Fig. 5 Thermogravimetry analysis (TGA) coupled with mass spectrometry (MS) of (a) a brittle-porous sample of TEDOT-C10-S-GNPs with 2 nm diameter GNPs (scheme in the inset) (b) the thin p(TEDOT) film on Si/Pt substrate (p(TEDOT) structure in the inset).

alkylthiol moiety as the reference in order to (i) maximize the thickness of the electropolymerized film by removing the electrically resistive part of the molecule and (ii) avoid the oxidation of the thiol group of the molecule during the electro-polymerization. We assume that the conclusions of these analyses on p(TEDOT) films are valid for the p(S-C10-TEDOT) systems.

The decomposition of the TEDOT moiety in **TEDOT-C10-S-GNP** starts occurring much earlier than that of **p(TEDOT)** which requires a high temperature of about 620 K (Fig. 5b). Both organic-based samples display one major mass loss, between 450 and 720 K for **TEDOT-C10-S-GNP** and between 620 K and 720 K for **p(TEDOT)**, involving the release of volatile species corresponding to numerous different ions detected by mass spectrometry. The mass spectrometry spectrum is shown only to emphasize the relationship between the mass losses recorded by TGA and the released gaseous species. As the quantity of organics is much lower than the one of gold particles and/or the silicon substrate, the decomposition of organic ligands does not produce a strong enough mass-spectrometry signal for the

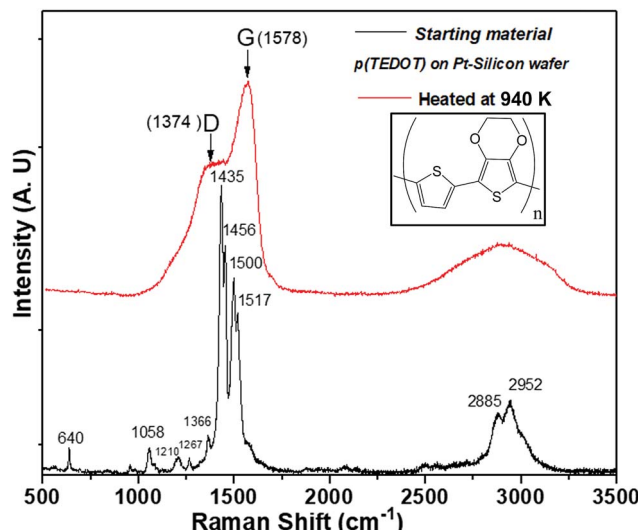


Fig. 6 Raman spectroscopy acquired from p(TEDOT) polymer deposited on Pt-silicon substrate before and after a thermal annealing in helium at 940 K.

assignment of the series of ions (*m/z*) to establish a clear-cut fragmentation pathway of evolved volatile molecules. Further work is clearly needed to clarify the decomposition mechanism of these materials.

As with many organic compounds, when **TEDOT-C10-S-GNPs** and **p(TEDOT)** are heated, the structural modification leads not only to volatile molecules, but also to a black residue called free carbon. **TEDOT-C10-S-GNP**s left a porous brittle black residue unsuitable for further analysis. However, the residue left on the silicon substrate from **p(TEDOT)**, which was easier to handle, has been characterized by Raman spectroscopy. Fig. 6 depicts the Raman spectra recorded from the polymer **p(TEDOT)** deposited on the Pt/Silicon wafer and the one thermally treated in helium at 940 K. In agreement with the literature,<sup>33-35</sup> the main Raman bands of the TEDOT moiety are observed in the spectrum and are listed in Table 1. As expected, the heated **TEDOT-C10-S-GNP**-based material exhibited the two characteristic broad C sp<sup>2</sup>-bands (band D at 1374 cm<sup>-1</sup> and band G at 1578 cm<sup>-1</sup>) of amorphous free carbon.

Table 1 Characteristic Raman frequencies of p(TEDOT) polymer

Wave number (cm <sup>-1</sup> )	Assignment of Raman bands
640	Oxyethylene ring deformation
1058	C–O–C deformation
1210	Stretching C <sub>α</sub> – C' <sub>α</sub> (inter-ring)
1267	Stretching C <sub>α</sub> – C' <sub>α</sub> (inter-ring), C <sub>β</sub> –H bending
1366	Stretching C <sub>β</sub> –C <sub>β</sub> intra-ring
1435	Symmetric stretching C <sub>α</sub> ≡C <sub>β</sub> (–O)
1456	Symmetric stretching C <sub>α</sub> ≡C <sub>β</sub> (–H)
1500	Asymmetric stretching C=C
1517	Asymmetric stretching C=C
2885	CH <sub>2</sub> stretching
2952	CH <sub>2</sub> stretching

## Temperature-dependent charge transport mechanisms

After the forming process, the device is set to the ON state by applying a double voltage sweep (amplitude from 0 to 20 and 20 to 0 V at  $4\text{ V s}^{-1}$ ), and in the OFF state by applying a single voltage sweep (0 to 20 V at  $4\text{ V s}^{-1}$ ) followed by an abrupt return to 0 V (Fig. 1a).<sup>3</sup> The charge transport properties of both states are characterized in the 80–300 K temperature range by measuring the ON and OFF current at a fixed reading bias of 1 V (Fig. 7). The Arrhenius plots for the ON and OFF currents show that the OFF current is weakly thermally activated with an activation energy of  $E_a = 51\text{ meV}$  above a threshold temperature of  $\sim 170\text{ K}$ , and not thermally activated below this temperature. The current in the ON state is not thermally activated in the 80 to 300 K temperature range. This behavior is similar to that previously reported for memory devices based on  $\text{TiO}_2$  nanoparticles embedded in poly(9-vinylcarbazole) films with no activation energy for the ON state, and an activation energy of  $\sim 66\text{ meV}$  for the OFF state at temperatures above 150 K.<sup>36</sup>

Several models of the charge transport mechanism could be suggested to explain the current–voltage ( $I$ – $V$ ) characteristics measured on the memory device, such as space charge limited current (SCLC), variable range hopping and thermionic emission limited conduction.<sup>37</sup>  $I$ – $V$  characteristics measured at 300 K in the OFF state (Fig. 8) are not consistent with the variable range hopping or thermionic emission limited conduction models (for details see the ESI†). In the case of the SCLC model, the  $I$ – $V$  curve in the log–log scale shows two distinct regions with different  $I$ – $V$  relationships (Fig. 8). From low voltages ( $<1\text{ V}$ ) in the OFF state the current increases linearly with the bias voltage (region 1). For voltages between 1 V and 10 V (region 2), the current exhibits a voltage square dependence. In the ON state, a linear relationship is observed from voltages up to 7 V. The  $I$ – $V$  characteristics in the OFF state are well explained by a SCLC mechanism according to the following two equations for low and high voltage regions respectively (from ref. 37):

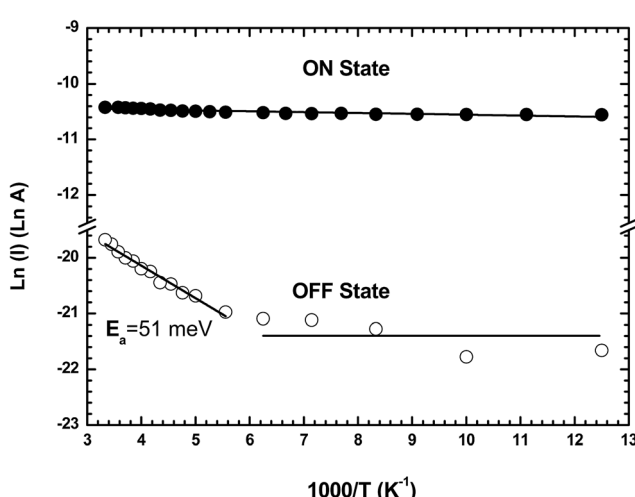


Fig. 7 Arrhenius plot of the current in the ON and OFF states in the temperature range from 80 to 300 K read at 1 V for a formed-pTEDOT-C10-S-GNP monolayer in a  $500\text{ nm} \times 1000\text{ }\mu\text{m}$  channel device.

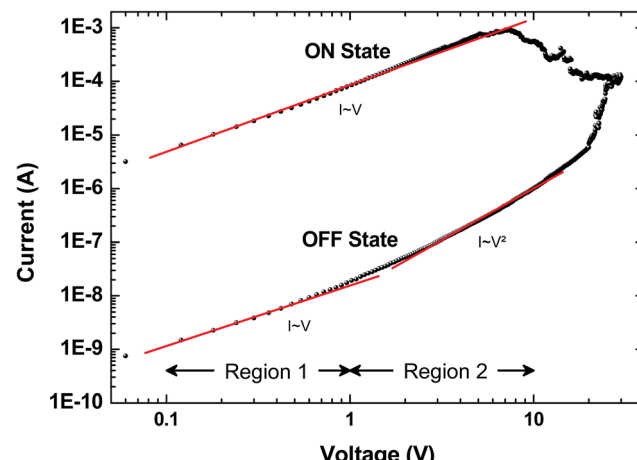


Fig. 8 Typical current  $I$  versus voltage  $V$  curves (log–log scale) for the memory behavior measured on a formed-pTEDOT-C10-S-GNP device with a  $1\text{ }\mu\text{m}$  gap length. Dots correspond to experimental data and red lines to the fitting adjustments before switching regions; *i.e.* in region 1 (0.1 to 1 V) and region 2 (1 to 10 V) for the OFF state, and from 0.1 to 7 V for the ON state. From these adjustments at low and high voltage and with eqn (1) and eqn (2), we estimate the density of trapped charge  $n_t \sim 1.6 \times 10^{14}\text{ cm}^{-3}$ .

$$I = S q \mu \frac{V}{s} \text{ (low voltage – weak injection)} \quad (1)$$

$$I = S \frac{9\mu\epsilon}{8s^3} \frac{n}{n_t} V^2 \text{ (higher voltage – strong injection)} \quad (2)$$

where  $I$  is the current,  $q$  is the electronic charge,  $n$  is the density of charge,  $\mu$  is the mobilité,  $V$  is the applied bias,  $s$  is the inter-electrode distance,  $\epsilon$  is the dielectric constant,  $n_t$  is the density of the trapped charge and  $S$  is the electrical contact surface. In the case of the ON state, the current is clearly ohmic. The same behavior is also observed for a shorter inter-electrode gap electrode of 500 nm (see Fig. SI-4†).

## Physical interpretation of the mechanism in the device

Cho *et al.*<sup>36</sup> observed that the ON state of memory devices based on  $\text{TiO}_2$  nanoparticles embedded in poly(9-vinylcarbazole) films followed an ohmic behavior and also observed a negligible temperature dependence of the current (*i.e.* no thermal activation). They concluded that the current in the ON state is mainly due to charge tunneling between filament conducting paths. Here the same features are observed. Thus, it is likely that the ON state of the device in this study corresponds to conduction through conducting pathways formed during the “forming process”. Based on the above SEM, STEM and Raman measurements, we conclude that the nature of these conducting paths is based on the hybrid material composed of amorphous  $\text{sp}^2$  carbon and gold clusters.

In the OFF state, we observed a weak thermal activation above 170 K and the  $I$ – $V$  characteristics are well explained by a trap-filled SCLC current model. Lin *et al.*<sup>12</sup> also observed SCLC behavior in the OFF state for devices composed of a layer of polystyrene mixed with GNPs of 2–5 nm diameter sandwiched

between two aluminum electrodes. As discussed in our previous work,<sup>3</sup> a charge carrier trapping/release mechanism from traps can explain these characteristics: (i) the ohmic behavior in the ON state corresponds to transport of free carriers in the hybrid material (see above); and (ii) the SCLC transport in the OFF state corresponds to injection limited transport when charge carriers are trapped in defects (traps) in the materials.

The physical mechanisms proposed here are close to that described by Simmons and Verderber in MIM structures in the 1960s, involving charge trapping/release and space charge field inhibition of injection.<sup>38</sup> The nature of the traps involved in the mechanism was generally associated to the NPs present in the hybrid organic/gold nanoparticle memories.<sup>3,7,8,10,12</sup> In the device presented here, after the forming process the resulting material is composed of gold clusters and amorphous sp<sup>2</sup> carbon. The gold clusters and amorphous sp<sup>2</sup> carbon can act as trapping centers. sp<sup>2</sup> carbon was suggested to be the trapping centers in hybrid poly(*N*-vinylcarbazole)-graphene nonvolatile memory devices.<sup>39</sup> Regarding the influence of the organic matrix on the electrical properties, the forming process induces an annealing of the organic matrix leading to the formation of amorphous sp<sup>2</sup> carbon. Moreover, we assume that switching and cluster formation can occur for other organic polymers incorporated into the device, but with some variation in the voltage values in the memory behavior due to the difference of gold diffusivity or sp<sup>2</sup> carbon formation for example.

## 4. Conclusions

Through the course of this study, we followed the physical mechanism involved in the forming process and operations of a hybrid memristive device based on a network of GNPs embedded in an electrogenerated pTEDOT matrix. The forming process leads to morphological modifications of the hybrid 2D monolayer film. Larger gold clusters of about 40 nm in diameter appear between the electrodes, similar to those obtained after thermal annealing of the GNP network at ~523 K. TG/MS and Raman analysis show evidence of changes in structural organic polymers. The resulting hybrid material, made of amorphous sp<sup>2</sup> carbon and gold clusters, is assumed to contain electrical traps, which can explain the voltage and temperature dependence of charge carrier transport in this device.

## Conflicts of interest

There are no conflicts to declare.

## Acknowledgements

This work has been financially supported by EU FET project no. 318597 "SYMONE", the ANR agency, project no. ANR 12 BS03 010 01 "SYNAPTOR" and the French RENATECH network. The authors thank the clean room staff of the IEMN for the assistance and help with device fabrication.

## References

- 1 F. Pan, S. Gao, C. Chen, C. Song and F. Zeng, Recent progress in resistive random access memories: materials, switching mechanisms, and performance, *Mater. Sci. Eng., R*, 2014, **83**, 1–59.
- 2 S. Gao, X. Yi, J. Shang, G. Liu and R.-W. Li, Organic and hybrid resistive switching materials and devices, *Chem. Soc. Rev.*, 2019, **48**, 1531–1565.
- 3 T. Zhang, D. Guérin, F. Alibart, D. Vuillaume, K. Lmimouni, S. Lenfant, A. Yassin, M. Ocafrain, P. Blanchard and J. Roncali, Negative Differential Resistance, Memory, and Reconfigurable Logic Functions Based on Monolayer Devices Derived from Gold Nanoparticles Functionalized with Electropolymerizable TEDOT Units, *J. Phys. Chem. C*, 2017, **121**(18), 10131–10139.
- 4 A. Yassin, M. Ocafrain, P. Blanchard, R. Mallet and J. Roncali, Synthesis of Hybrid Electroactive Materials by Low-Potential Electropolymerization of Gold Nanoparticles Capped with Tailored EDOT-Thiophene Precursor Units, *ChemElectroChem*, 2014, **1**(8), 1312–1318.
- 5 L. Ma, J. Liu and Y. Yang, Organic electrical bistable devices and rewritable memory cells, *Appl. Phys. Lett.*, 2002, **80**(16), 2997–2999.
- 6 R. J. Tseng, J. Huang, J. Ouyang, R. B. Kaner and Y. Yang, Polyaniline nanofiber/gold nanoparticle nonvolatile memory, *Nano Lett.*, 2005, **5**(6), 1077–1080.
- 7 A. Prakash, J. Ouyang, J.-L. Lin and Y. Yang, Polymer memory device based on conjugated polymer and gold nanoparticles, *J. Appl. Phys.*, 2006, **100**(5), 054309.
- 8 L. D. Bozano, B. W. Kean, M. Beinhoff, K. R. Carter and J. C. Scott, *Adv. Funct. Mater.*, 2005, **15**, 1933.
- 9 J. Li, A. Tang, X. Li, Y. Cao, M. Wang, Y. Ning, L. Lv, Q. Lu, Y. Lu, Y. Hu, Y. Hou and F. Teng, Negative differential resistance and carrier transport of electrically bistable devices based on poly(*N*-vinylcarbazole)-silver sulfide composites, *Nanoscale Res. Lett.*, 2014, **9**, 128.
- 10 D. I. Son, D. H. Park, J. Bin Kim, J. W. Choi, T. W. Kim, B. Angadi, Y. Yi and W. K. Choi, Bistable Organic Memory Device with Gold Nanoparticles Embedded in a Conducting Poly(*N*-vinylcarbazole) Colloids Hybrid, *J. Phys. Chem. C*, 2011, **115**(5), 2341–2348.
- 11 J. Y. Ouyang, Materials effects on the electrode-sensitive bipolar resistive switches of polymer: gold nanoparticle memory devices, *Org. Electron.*, 2013, **14**(6), 1458–1466.
- 12 H.-T. Lin, Z. Pei and Y.-J. Chan, Carrier transport mechanism in a nanoparticle-incorporated organic bistable memory device, *IEEE Electron Device Lett.*, 2007, **28**(7), 569–571.
- 13 G. Casula, P. Cosseddu, Y. Busby, J.-J. Pireaux, M. Rosowski, B. T. Szczesna, K. Soliwoda, G. Celichowski, J. Grobelny, J. Novak, R. Banerjee, F. Schreiber and A. Bonfiglio, Air-stable, non-volatile resistive memory based on hybrid organic/inorganic nanocomposites, *Org. Electron.*, 2015, **18**, 17–23.



14 D. Tondelier, K. Lmimouni, D. Vuillaume, C. Fery and G. Haas, Metal/organic/metal bistable memory devices, *Appl. Phys. Lett.*, 2004, **85**(23), 5763–5765.

15 L. D. Bozano, B. W. Kean, V. R. Deline, J. R. Salem and J. C. Scott, Mechanism for bistability in organic memory elements, *Appl. Phys. Lett.*, 2004, **84**(4), 607–609.

16 Y. Busby, N. Crespo-Monteiro, M. Girleanu, M. Brinkmann, O. Ersen and J.-J. Pireaux, 3D imaging of filaments in organic resistive memory devices, *Org. Electron.*, 2015, **16**, 40–45.

17 G. Casula, Y. Busby, A. Franquet, V. Spampinato, L. Houssiau, A. Bonfiglio and P. Cosseddu, A flexible organic memory device with a clearly disclosed resistive switching mechanism, *Org. Electron.*, 2019, **64**, 209–215.

18 M. Ocafraín, T. K. Tran, P. Blanchard, S. Lenfant, S. Godey, D. Vuillaume and J. Roncali, Electropolymerized self-assembled monolayers of a 3,4-ethylenedioxythiophene-thiophene hybrid system, *Adv. Funct. Mater.*, 2008, **18**(15), 2163–2171.

19 F. Wang, C. He, M.-Y. Han, J. H. Wu and G. Q. Xu, Chemical controlled reversible gold nanoparticles dissolution and reconstruction at room-temperature, *Chem. Commun.*, 2012, **48**(49), 6136–6138.

20 C. Shen, C. Hui, T. Yang, C. Xiao, J. Tian, L. Bao, S. Chen, H. Ding and H. Gao, Monodisperse Noble-Metal Nanoparticles and Their Surface Enhanced Raman Scattering Properties, *Chem. Mater.*, 2008, **20**(22), 6939–6944.

21 H. Hiramatsu and F. E. Osterloh, A simple large-scale synthesis of nearly monodisperse gold and silver nanoparticles with adjustable sizes and with exchangeable surfactants, *Chem. Mater.*, 2004, **16**(13), 2509–2511.

22 Y. Viero, G. Copie, D. Guerin, C. Krzeminski, D. Viiillaume, S. Lenfant and F. Cleri, High Conductance Ratio in Molecular Optical Switching of Functionalized Nanoparticle Self-Assembled Nanodevices, *J. Phys. Chem. C*, 2015, **119**(36), 21173–21183.

23 V. Santhanam, J. Liu, R. Agarwal and R. P. Andres, Self-assembly of uniform monolayer arrays of nanoparticles, *Langmuir*, 2003, **19**(19), 7881–7887.

24 Y. Yang, P. Gao, L. Li, X. Pan, S. Tappertzhofen, S. Choi, R. Waser, I. Valov and W. D. Lu, Electrochemical dynamics of nanoscale metallic inclusions in dielectrics, *Nat. Commun.*, 2014, **5**, 4232.

25 D. R. Lyde, *Handbook of Chemistry and Physics*, CRC Press, Boca Raton, 74th edn, 1993, pp. 1993–1994.

26 P. Buffat and J. P. Borel, Size effect on melting temperature of gold particles, *Phys. Rev. A: At., Mol., Opt. Phys.*, 1976, **13**(6), 2287–2298.

27 L. J. Lewis, P. Jensen and J. L. Barrat, Melting, freezing, and coalescence of gold nanoclusters, *Phys. Rev. B: Condens. Matter Mater. Phys.*, 1997, **56**(4), 2248–2257.

28 T. Shimizu, T. Teranishi, S. Hasegawa and M. Miyake, Size evolution of alkanethiol-protected gold nanoparticles by heat treatment in the solid state, *J. Phys. Chem. B*, 2003, **107**(12), 2719–2724.

29 K. Dick, T. Dhanasekaran, Z. Zhang and D. Meisel, Size-Dependent Melting of Silica-Encapsulated Gold Nanoparticles, *J. Am. Chem. Soc.*, 2002, **124**(10), 2312–2317.

30 Y. Yang, P. Gao, S. Gaba, T. Chang, X. Pan and W. Lu, Observation of conducting filament growth in nanoscale resistive memories, *Nat. Commun.*, 2012, **3**, 732.

31 Y. Yang, B. Chen and W. D. Lu, Memristive Physically Evolving Networks Enabling the Emulation of Heterosynaptic Plasticity, *Adv. Mater.*, 2015, **27**(47), 7720–7727.

32 M. Turbiez, P. Frère, P. Blanchard and J. Roncali, Mixed  $\pi$ -conjugated oligomers of thiophene and 3,4-ethylenedioxythiophene (EDOT), *Tetrahedron Lett.*, 2000, **41**(29), 5521–5525.

33 P. Larkin, *Infrared and Raman Spectroscopy*, Elsevier, Oxford, 2011.

34 J. L. Duvail, P. Retho, S. Garreau, G. Louarn, C. Godon and S. Demoustier-Champagne, Transport and vibrational properties of poly(3,4-ethylenedioxythiophene) nanofibers, *Synth. Met.*, 2002, **131**(1–3), 123–128.

35 S. Garreau, J. L. Duvail and G. Louarn, Spectroelectrochemical studies of poly(3,4-ethylenedioxythiophene) in aqueous medium, *Synth. Met.*, 2001, **125**(3), 325–329.

36 B. Cho, T. W. Kim, M. Choe, G. Wang, S. Song and T. Lee, Unipolar nonvolatile memory devices with composites of poly(9-vinylcarbazole) and titanium dioxide nanoparticles, *Org. Electron.*, 2009, **10**(3), 473–477.

37 P. Hesto, The nature of electronic conduction in thin insulating layers, in *Instabilities in Silicon Devices*, ed. G. Barbottin and A. Vapaille, Elsevier, Amsterdam, 1986, vol. 1, pp. 263–314.

38 J. G. Simmons and R. Verderbe, New Conduction and Reversible Memory Phenomena in Thin Insulating Films, *Proc. Roy. Soc. Lond. Math. Phys. Sci.*, 1967, **301**(1464), 77–102.

39 Q. Zhang, J. Pan, X. Yi, L. Li and S. Shang, Nonvolatile memory devices based on electrical conductance tuning in poly(N-vinylcarbazole)-graphene composites, *Org. Electron.*, 2012, **13**(8), 1289–1295.

